PCCP

Accepted Manuscript




ROYAL SOCIETY OF CHEMISTRY

www.rsc.org/pccp

# Mesoporous $ZnCo_2O_4$ nanoflakes grown on nickel foam as electrodes for high performance supercapacitors

Jinbing Cheng,[†a,b] Yang Lu,[†a,b,c] Kangwen Qiu,[†a,b] Hailong Yan,[a,b] Xiaoyi Hou,[a,b] Jinyou Xu,[a,b] Lei Han,[a] Xianming Liu,[d] Jang-Kyo Kim[e] and Yongsong Luo[*a,b]

[a]*School of Physics and Electronic Engineering, Xinyang Normal University, Xinyang 464000, P. R. China.*

[b]*Key Laboratory of Advanced Micro/Nano Functional Materials, Xinyang Normal University, Xinyang 464000, P. R. China.*

[c]*School of Material Science and Engineering, Hebei University of Technology, Tianjin 300130, P. R. China.*

[d]*College of Chemistry and Chemical Engineering, Luoyang Normal University, Luoyang 471022, P. R. China.*

[e]*Department of Mechanical and Aerospace Engineering, The Hong Kong University of Science and Technology, Clear Water Bay, Kowloon, Hong Kong, P. R. China.*

**Abstract:** $ZnCo_2O_4$ nanoflakes are grown on a cellular nickel foam using a cost effective hydrothermal procedure as electrodes for supercapacitors. The mesoporous $ZnCo_2O_4$ nanoflakes have large electroactive surface areas with strong adhesion with the Ni foam, allowing fast ion and electron transport. The nanoarchitecture electrodes deliver an excellent specific capacitance of 1220 F $g^{-1}$ at a current density of 2 A $g^{-1}$ in a 2 M KOH aqueous solution and a long-term cyclic stability of 94.2% capacitance

* To whom correspondence should be addressed：Tel/Fax: +86-376-6390801;
E-mail: ysluo@xynu.edu.cn

† These authors contribute equally to this work.

retention after 5000 cycles. The fabrication strategy is facile, cost-effective, and can offer great promise for large-scale supercapacitor applications.

**Key words:** Spinel zinc cobaltate, mesoporous, nanoflake, supercapacitor

## 1. Introduction

As energy storage devices with properties intermediate to those of batteries and electrostatic capacitors, electrochemical supercapacitors (SCs) possess many desirable properties. They include high power densities of ten times higher than batteries, extremely fast charging time within seconds, excellent cyclic stability, small size and low mass, making SCs one of the most promising candidates for next-generation power devices.[1-7] With characteristics complementary to those of rechargeable batteries and fuel cells, SCs have been used in many applications, such as power back-up, pacemakers, air bags and electrical vehicles.[8] The electrode material is a key component that determines the SC's functional performance. An excellent electrode material for pseudocapacitors is $RuO_x$, due to an ideal capacitive behavior, a large specific area, high conductivity and electrochemical stability.[9] However, the hydrated $RuO_x$ is expensive and toxic, which limits its practical applications for SCs.[10] Therefore, alternative materials with superior pseudocapacitive characteristics need to be identified. Inexpensive transitional metal oxides, such as ZnO,[11] $Co_3O_4$,[12,13] $MnO_2$,[14,15] NiO,[16,17] and $SnO_2$,[18] have thus far been studied as the electrode material for pseudocapacitors. The exploration of electrode materials with higher power performance and longer cyclic life for pseudocapacitors is still in great need.[19]

Many research efforts have recently been directed towards preparation of binary

compounds for SCs.[20-23] Spinel cobaltite $ZnCo_2O_4$ is known be efficient for oxygen reduction when used as an electrode, and is low cost, abundant and environment friendly.[24] $ZnCo_2O_4$ has been developed for applications in Li-ion batteries,[25,26] electrocatalysts[27,28] and SCs,[29-31] demonstrating its multi-functionalities. It was revealed that both the $NiCo_2O_4$ and $ZnCo_2O_4$ electrodes delivered superior capacitive performance to $Co_3O_4$ because of their stronger electrochemical activities and richer redox reactions than the latter.[32-34]

Herein, we demonstrate a simple yet high efficiency approach for preparing porous hexagonal $ZnCo_2O_4$ nanoflakes using a one-step hydrothermal method coupled with an annealing treatment. The $ZnCo_2O_4$ nanoflakes grown directly on a nickel foam can avoid the use of polymer binders and conducting additives, thus excellent mechanical adhesion and electrical connection are ensured. Through electrochemical measurements, the $ZnCo_2O_4$ nanoflakes are found to be a promising pseudocapacitive material with a high specific capacitance and excellent rate capability.

## 2. Experimental

### 2.1 Synthesis of mesoporous $ZnCo_2O_4$ nanoflakes

All the reagents were analytical grade and directly used without further purification. Prior to deposition, nickel foams of 1.5 cm × 4.0 cm in rectangular shape were cleaned by sonication in acetone, 1 M HCl solution, deionized (DI) water, and ethanol for 15 min each. Nanoflakes were grown on the nickel foam via a simple one-pot hydrothermal process. 1 mmol (0.30 g) of $Zn(NO_3)_2 \cdot 6H_2O$ and 2 mmol (0.58 g) of $Co(NO_3)_2 \cdot 6H_2O$ were dissolved into 35 mL of DI water and 5 mL of ethanol absolute,

followed by the addition of 15 mmol (0.90 g) of urea and 6 mmol (0.22 g) of $NH_4F$ at room temperature, and the mixture was stirred to form a clear pink solution. Then the mixture was transferred to a 50 mL Teflon-lined stainless steel autoclave. The cleaned Ni foam was immersed in the mixture, and the autoclave was kept at 120 $^oC$ for 6 h. After cooling down to room temperature, the Ni foam was taken out and washed with DI water and ethanol several times to obtain Zn-Co hydroxide precursor on its surface. The as-prepared precursor was annealed at 400 $^oC$ in air for 2 h at a ramping rate of 1 $^oC\ min^{-1}$ to obtain hexagon-shaped $ZnCo_2O_4$ nanoflakes. For comparison, $Co_3O_4$ was also prepared using $Co(NO_3)_2 \cdot 6H_2O$ as the reactant under the same procedure.

**2.2 Materials characterization**

The crystalline structure and phase purity of the products were identified by X-ray diffraction (XRD) analysis on a D8 Advance (Bruker) automated X-ray diffractometer system with Cu-Kα (λ = 1.5418 Å) radiation at 40 kV and 40 mA, and 2θ ranging from 10° to 80° at room temperature. Raman spectroscopy was carried out using an INVIA Raman microprobe (Renishaw Instruments) with a 532 nm laser source and a 50× objective lens. The morphologies and structures were examined on a field emission scanning electron microscope (FESEM, JEOL S-4800) and a transmission electron microscope (TEM, JEOL JEM-2010). The elemental analysis was carried out using an energy-dispersive X-ray spectroscope (EDS, Bruker-QUANTAX) attached to the FESEM. The Brunauer-Emmett-Teller (BET) surface areas of the electrode materials of 45 mg in weight were determined using the nitrogen sorption/desorption isotherms obtained at 77K from a surface area and porosity analyzer (Quadrasorb

SI-MP, Quantachrome). The chemical elements of the electrodes were analyzed on a X-ray photoelectron spectroscopy (XPS, Perkin-Elmer PHI 5600 XPS system).

**2.3 Electrochemical measurements**

The electrochemical properties of the products were studied based on cyclic voltammetry (CV), electrochemical impedance spectroscopy (EIS) tests and galvanostatic charge/discharge (GCD) curves using three-electrode cells on a electrochemical workstation (CHI 660E). The three-electrode cell contained a Pt foil as the counter electrode, a standard calomel electrode (SCE) as the reference electrode, $ZnCo_2O_4$ nanoflakes (m≈ 10 mg) and as-prepared $Co_3O_4$ (m≈ 8 mg) grown on a nickel foam as the working electrode, with a solution of 2 M KOH as the electrolyte. The CV analysis was performed between 0 and 0.6 V vs. SCE at scan rates ranging from 5 to 50 mV $s^{-1}$. The GCD tests were conducted in a stable potential window between 0 and 0.6 V at different current densities of 2-10 A $g^{-1}$ on a LAND battery program-control test system. The EIS measurements were made by applying an AC voltage with 10 mV amplitude in a frequency range from 0.01 Hz to 100 kHz. The nominal area of these electrodes immersed into the electrolyte was controlled to be around 1.0 cm × 3.0 cm. The specific capacitance, C (F $g^{-1}$), was calculated according to the following equation:

$$C = \frac{I\Delta t}{M\Delta v} \quad (1)$$

where $I$ (mA) represents the discharge current, and $M$ (mg), $\Delta V$ (v) and $\Delta t$ (s) refer to the mass of active material, potential drop during discharge and total discharge time, respectively.

## 3. Results and discussion

### 3.1 Morphology and structure of $ZnCo_2O_4$

Fig. 1 illustrates the design and synthesis strategy of $ZnCo_2O_4$ on a Ni foam as an electrode material. The whole process involved two steps: firstly, the Zn-Co hydroxide precursor in the form of nanoflake coating was uniformly grown on the Ni foam via a facile, hydrothermal process; and secondly, $ZnCo_2O_4$ was obtained after annealing in air while maintaining the hexagonal structure.

Fig. 2 shows the XRD patterns of the mesoporous $ZnCo_2O_4$ nanoflakes and $Co_3O_4$ supported on a Ni foam. Except for the peaks originating from the Ni foam substrate, all the diffraction peaks can be indexed to a cubic phase of $ZnCo_2O_4$ (JCPDS card No. 01-1149).[28] The composition and structure of the $ZnCo_2O_4$ were further confirmed by the Raman analysis, as shown in Fig. S1. Four prominent peaks were observed at 183, 481.2, 523.4 and 625.7 $cm^{-1}$, which are assigned to $F_{2g}$, $E_g$, $F_{2g}$ and $A_{1g}$ models of $ZnCo_2O_4$, respectively. Only the Co-O and Zn-O vibrations were detected and signals from the OH group were absent, indicating that the precursor cobalt/zinc metallic carbonate hydroxide salts were completely decomposed after calcination at 400 $^oC$. These results are consistent with those reported previously.[35] Fig. S2 gives the thermogravimetric and differential thermal analysis (TG-DTA) curves of the Zn-Co hydroxide precursor in air, showing the beginning of decomposition at ~208 $^oC$ after the evaporation of water and other small molecular species. In the DTA curve, there was a strong heat absorption peak at ~394 $^oC$, originating from the decomposition of Zn-Co hydroxide to $ZnCo_2O_4$. These observations demonstrate that the annealing

temperature, 400 $^{o}$C, chosen in this study was appropriate.

The SEM images of $ZnCo_2O_4$ taken at increasingly higher magnifications are shown in Fig. 3. The nanoflakes were grown over the whole Ni foam skeleton to form a large-scale, uniform coating (Fig. 3a). The higher magnification SEM image (Fig. 3b) shows that the products are highly compact and intertwined in a cluster, resembling blooming flowers. Fig. 3c, d display that the nanoflakes lie aslant to the Ni foam support and are interconnected with each other, forming a highly open nanochannel. Thus, most of the nanoflake surfaces are accessible by the electrolyte when used as an electrode for SCs. Of particular note is that the diameter of as-synthesized $ZnCo_2O_4$ nanoflakes is approximately 6-7 μm. For comparison, the SEM images of the $Co_3O_4$ composed of many overlapping nanosheets are also shown in Fig. S3.

More detailed information about the morphological and structural features of the as-synthesized $ZnCo_2O_4$ nanoflakes is gained by TEM, HRTEM and selected-area electron diffraction (SAED). Fig. 4a, b display a bundle of nanoflakes with hexagon profiles. The selected-area electron diffraction (SAED) pattern (the inset in Fig. 4a) shows well-defined rings with polycrystalline characteristics, which are readily indexed to the (111), (220) and (311) planes of the cubic $ZnCo_2O_4$ phase, respectively, consistent with the above XRD results. The HRTEM image (Fig. 4c) presents that the lattice fringes were ~0.249 and 0.482 nm, corresponding to the (311) and (111) planes of spinel structured $ZnCo_2O_4$, respectively.[36] The EDS spectrum (Fig. 4d) presents O, Co and Zn elements with the atomic ratio of Co to Zn being approximately 2:1.

The XPS general spectrum (Fig. 5a) indicates the presence of Zn, Co and O elements in the $ZnCo_2O_4$ nanoflakes. The Zn 2p deconvoluted spectrum (Fig. 5b) presents strong peaks at 1020.2 and 1044.4 eV, attributed to Zn $2p_{1/2}$ and Zn $2p_{3/2}$, respectively. Two major peaks at binding energies of 780.3 and 795.7 eV were observed from the complex Co 2p spectrum (Fig. 5c), arising from the Co $2p_{3/2}$ and Co $2p_{1/2}$ spin-orbit peaks, respectively. The O 1s detailed spectrum (Fig. 5d) was resolved into two components, centered at 530.4 and 531.8 eV, which are attributed to the $O^{2-}$ forming oxide with Co and Zn elements, and $OH^-$, respectively,.

The porous structure of $ZnCo_2O_4$ nanoflakes needs a special mention because of the importance of pores and surface area in electrodes for SCs. The porous structure enables facile transport of the electrolyte to the surface of $ZnCo_2O_4$ nanoflakes, resulting in rapid charge transfer reactions due to the shortened ion diffusion paths. It is thought that the annealing process helped the formation of pores within the nanoflake clusters when the gas was released during the decomposition of the Zn-Co hydroxide precursor. Fig. S4 shows type IV adsorption/desorption isotherms with type H3 hysteresis loops according to the IUPAC (International Union of Pure and Applied Chemistry) classifications of hysteresis loops,[37] a reflection of a typical mesoporous microstructure.[38,39] After a steady increase, the adsorbed nitrogen volume surged at a relative pressure close to unity, implying the existence of large interconnected voids or void space within the nanoflakes. The pore size distribution (PSD) data (inset of Fig. S4) show that the majority of the pores fell in the range of 6-10 nm, which is known to be optimal for SC applications. The mesoporous structure gave rise to a

high porosity of 0.22 $cm^3$ $g^{-1}$ and a large BET specific surface area of 117 $m^2$ $g^{-1}$.

### 3.2 Electrochemical behavior of $ZnCo_2O_4$ nanoflakes

Fig. 6a shows the CV of the $ZnCo_2O_4$ nanoflake electrode in comparison with those of the $Co_3O_4$ and neat Ni foam electrodes determined at a scan rate of 30 mV $s^{-1}$. The signal from the Ni foam electrode was negligible compared to the other CVs. The area integrated from the current-potential curve of the $ZnCo_2O_4$ electrode was significantly larger than that of the $Co_3O_4$ electrode, indicating stronger electrochemical reaction activities of the former. Fig. 6b presents the cyclic voltammograms of the $ZnCo_2O_4$ electrode within the potential range of 0 to 0.6 V (vs. SCE) at various scan rates from 5 to 50 mV $s^{-1}$. Clearly, when the scan rate was 5 mV $s^{-1}$, a distinct pair of redox peaks were observed, indicating that the energy storage mechanism of the $ZnCo_2O_4$ electrode originated mainly from faradaic redox reactions assigned to the $Co(OH)_2$/CoOOH redox couple prior to the onset of oxygen evolution.[40,41] When the scan rate increased from 5 to 50 mV $s^{-1}$, the corresponding current enhanced while the shape of the CV curves remained largely unchanged, except for the shifts of the peak positions. The galvanostatic charge/discharge curves (Fig. 6c) had nearly symmetrical, nonlinear triangular shapes, confirming a high and reversible charge storage capacity of the electrode.[42] The $ZnCo_2O_4$ nanoflake electrode showed remarkable specific capacitances of 1220 F $g^{-1}$ (2 A $g^{-1}$), 1142 F $g^{-1}$ (4 A $g^{-1}$), 1074 F $g^{-1}$ (6 A $g^{-1}$), 973 F $g^{-1}$ (8 A $g^{-1}$) and 881 F $g^{-1}$ (10 A $g^{-1}$), respectively, which are compared with the corresponding values of the $Co_3O_4$ electrode, as shown in Fig. 6d. It is obvious that the specific capacitances of the former electrode were about 500 F $g^{-1}$ higher than

those of the latter electrode for a given current density. The comparison of the capacitances between the current study and similar metal oxide electrodes taken from the literature is shown in Table S1. The capacitance delivered by the $ZnCo_2O_4$ nanoflake electrode in this study is proven to be among the best, confirming that the design of $ZnCo_2O_4$ nanoflakes with a mesoporous structure is efficient for SC applications.

The long-term cyclic stability of SCs is another critical issue in practical use. Cyclic tests were carried out for over 5000 cycles at 2 A $g^{-1}$. Fig. 7a presents that the $ZnCo_2O_4$ nanoflake electrode exhibited an excellent long-term stability with only 5.8% capacitance loss after 5000 cycles, which is much better than 13.4% capacitance loss by the $Co_3O_4$ electrode. After charging/discharging 5000 cycles, the $ZnCo_2O_4$ nanoflakes showed little structural changes (as shown in Fig. S5). High rate capabilities were measured at progressively increasing current densities, as shown in Fig. 7b. In the first 300 cycles at 2 A $g^{-1}$, the specific capacitance of the $ZnCo_2O_4$ electrode slightly dropped from 1220 to 1208 F $g^{-1}$ and then stabilized. Even after sudden upward changes in current density, the $ZnCo_2O_4$ electrode delivered very stable specific capacitances. Upon reverting to 2 A $g^{-1}$ after 1500 charge/discharge cycles, the $ZnCo_2O_4$ electrode sustained exceptional 98% of the initial capacitance, which is well compared with 91% of the $Co_3O_4$ electrode.

The ion diffusion and electron transfer in the two electrode materials were evaluated using the EIS measurements (Fig. 7c). The two impedance spectra were similar, all composed of one semicircle component at a high frequency range and a linear component at a low frequency range. The internal resistance ($R_s$) is the sum of

the ionic resistance of electrolyte, the intrinsic resistance of active materials and the contact resistance at the active material/current collector interface,[43] and can be obtained from the intercept of the plots on the real axis. The semicircle of Nyquist plot corresponds to the Faradic reactions and its diameter represents the interfacial charge transfer resistance ($R_{ct}$). The inset of Fig. 7c showed an equivalent circuit used to fit the EIS curves to measure $R_s$ and $R_{ct}$, where $Z_w$ and CPE are the Warburg impendence and the constant phase element, respectively.[44] The fitting results are shown in Table S2, confirming much lower $R_s$ and $R_{ct}$ values of the $ZnCo_2O_4$ electrode than the $Co_3O_4$ electrode. Furthermore, the $ZnCo_2O_4$ electrode presented a higher slope and a shorter line in the low frequency region, suggesting a faster $OH^-$ diffusion rate and a smaller variation of diffusion paths. The $R_{ct}$ increased by only 0.8 Ω after 5000 cycles confirming that the $ZnCo_2O_4$ nanoflake structure was well preserved, consistent with the very stable cyclic performance (Fig. 7a). The excellent electrochemical performance of $ZnCo_2O_4$ nanoflakes may be attributed to their unique microstructures. First, the nanoflakes were intertwined with each other and directly attached to the substrate, which increased the effective contact area between electrode and electrolyte and improved the utilization of active materials. Second, the unique porous structure of nanoflakes further increased the electroactive sites for the Faradic reactions, and shortened the distance of $OH^-$ ion/electron transformation, which led to faster kinetics and enhanced the electrochemical performance. The direct growth of $ZnCo_2O_4$ nanoflakes onto the highly conductive Ni foam substrate means participation of the majority of the highly porous electrode materials in the ultrafast electrochemical reaction, as schematically shown in Fig. 7d. These findings demonstrate that the combination of fast ion diffusion and low electron transfer resistance resulted in enhanced electrochemical performance. In addition, the

interconnected network of $ZnCo_2O_4$ nanoflakes directly grown on a Ni foam substrate assured good mechanical adhesion to the underneath current collector and excellent electrical conductivities.[45] Along with these ameliorating structural features, the freestanding nature of the electrode allowed fast electron/ion transport without the needs of conductive additives or polymer binder which usually add extra interfacial resistance.

## 4. Conclusions

In summary, this paper presents a facile and highly-efficient hydrothermal method for direct growth of mosoporous hexagonal $ZnCo_2O_4$ coatings on a Ni foam substrate. The synthesis route was robust and scalable so that the technique may be extended to fabricate other nanostructures for various applications in electrochemical energy storage devices. Several unique structural features and ameliorating properties are considered responsible for the excellent electrochemical performance of the $ZnCo_2O_4$ electrode. (i) The direct growth of freestanding $ZnCo_2O_4$ nanoflakes on a highly conductive Ni foam substrate means total elimination of polymer binders and conductive additives, substantially reducing the "dead volume" in the electrode. (ii) The direct growth also ensured outstanding mechanical adhesion and electrical conduction to the current collector. (iii) The unique three dimensional mesoporous nanoflake architecture with a very large surface area and porosity offered faster ion/electron transfer, an improved reactivity and an enhanced electrochemical kinetics.

## Acknowledgments

This work was financially supported by the National Natural Science Foundation of

China (Nos. U1204501, U1304108 and 21373107), the Innovative Research Team (in Science and Technology) in University of Henan Province (No. 13IRTSTHN018) and University Students Sustentation Fund of Xinyang Normal University (No. 2014KYJJ30).

## References

1 J. R. Miller, R. A. Outlaw and B. C. Holloway, *Science*, 2010, **329**, 1637-1639.

2 D. Guo, Y. Z. Luo, X. Z. Yu, Q. H. Li and T. H. Wang, *Nano Energy*, 2014, **8**, 147-182.

3 Y. S. Luo, J. S. Luo, J. Jiang, W. W. Zhou, H. P. Yang, X. Y. Qi, H. Zhang, H. J. Fan, D. Y. W. Yu, C. M. Li and T. Yu, *Energy Environ. Sci*., 2012, **5**, 6559-6566.

4 J. M. Tarascom and M. Armand, *Nature*, 2001, **414**, 359-367.

5 F. Zhang, C. Z. Yuan, X. J. Lu, L. J. Zhang, Q. Che and X. G. Zhang, *J. Power Sources*, 2012, **203**, 250-256.

6 J. P. Liu, J. Jiang, C. W. Cheng, H. X. Li, J. X. Zhang, H. Gong and H. J. Fan, *Adv. Mater*., 2011, **23**, 2076-2081.

7 Y. Lu, H. L. Yan, K. W. Qiu, J. B. Cheng, W. X. Wang, X. M. Liu, C. C. Tang, J. K. Kim and Y. S. Luo, *RSC Adv*., 2015, **5**, 10773-10781.

8 J. R. Miller and P. Simon, *Science*, 2008, **321**, 651-652.

9 Z. S. Wu, D. W. Wang, W. Ren, J. Zhao, G. Zhou, F. Li and H. M. Cheng, *Adv Funct. Mater*., 2010, **10**, 3595-3602.

10 J. W. Lee, A. S. Hall, J. D. Kim and T. E. Mallouk, *Chem. Mater*., 2012, **24**, 1158-1164.

11 J. Bae, M. K. Song, Y. J. Park, J. M. Kim, M. Liu and Z. L. Wang, *Angew. Chem. Int. Ed*., 2011, **50**, 1-6.

12 X. X. Qing, S. Q. Liu, K. L. Huang, K. Z. Lv, Y. P. Yang, Z. G. Lu, D. Fang and X. X. Liang, *Electrochim. Acta*, 2011, **56**, 4985-4991.

13 X. W. Lou, D. Deng, J. Y. Lee, J. Feng and L. A. Archer, *Adv. Mater*., 2008, **20**, 258-262.

14 H. Jiang, T. Zhao, C. Y. Yan, J. Ma and C. Z. Li, *Nanoscale*, 2010, **2**, 2195-2198.

15 M. Fang, X. L. Tan, M. Liu, S. H. Kang, X. Y. Hu and L. D. Zhang, *CrystEngComm*, 2011, **13**, 4915-4920.

16 J. H. Kim, K. Zhu, Y. F. Yan, C. L. Perkins and A. J. Frank, *Nano Lett*., 2010, **10**, 4099-4104.

17 G. H. Zhang, Y. J. Chen, B. H. Qu, L. L. Hu, L. Mei, D. L. Lei, Q. Li, L. B. Chen, Q. H. Li and T. H. Wang, *Electrochim. Acta*, 2012, **80**, 140-147.

18 R. K. Selvan, I. Perelshtein, N. Perkas and A. Gedanken, *J. Phys. Chem. C*, 2008, **112**, 1825-1830.

19 M. F. Shao, F. Y. Ning, Y. F. Zhao, J. W. Zhao, M. Wei, D. G. Evans and X. Duan, *Chem. Mater*., 2012, **24**, 1192-1197.

20 H. W. Wang, Z. A. Hu, Y. Q. Chang, Y. L. Chen, H. Y. Wu, Z. Y. Zhang and Y. Y. Yang, *J. Mater. Chem*., 2011, **21**, 10504-10511.

21 Z. W. Xu, Z. Li, X. H. Tan, C. M. B. Holt, L. Zhang, B. S. Amirkhiz and D. Mitlin, *RSC Adv*., 2012, **2**, 2753-2755.

22 J. F. Zang, L. H. Bao, R. A. Webb and X. D. Li, *Nano Lett*., 2011, **11**, 4885-4889.

23 B. Liu, B. Y. Liu, Q. F. Wang, X. F. Wang, Q. Y. Xiang, D. Chen and G. Z. Shen, *ACS Appl. Mater. Interfaces*, 2013, **5**, 10011-10017.

24 K. W. Qiu, Y. Lu, D. Y. Zhang, J. B. Cheng, H. L. Yan, J. Y. Xu, X. M. Liu, J. K. Kim and Y. S. Luo, *Nano Energy*, 2015, **11**, 687-696.

25 B. Liu, D. S. Tan, X. F. Wang, D. Chen and G. Z. Shen, *Small*, 2013, **9**, 1998-2004.

26 S. B. Wang, J. Pu, Y. Tong, Y. Y. Cheng, Y. Gao and Z. H. Wang, *J. Mater. Chem. A*, 2014, **2**, 5434-5440.

27 B. Chi, J. B. Li, X. Z. Yang, H. Lin and N. Wang, *Electrochim. Acta*, 2015, **50**, 2059-2064.

28 Z. H. Pu, Q. Lian, C. Tang, A. M. Asiri, A. H. Qusti, A. O. Al-Youbi and X. P. Sun, *J. Power Sources*, 2014, **257**, 170-173.

29 G. Zhou, J. Zhu, Y. J. Chen, L. Mei, X. C. Duan, G. H. Zhang, L. B. Chen, T. H. Wang and B. G. Lu, *Electrochim. Acta*, 2014, **123**, 450-455.

30 H. Wu, Z. Lou, H. Yang and G. Z. Shen, *Nanoscale*, 2015, **7**, 1921-1926.

31 K. Karthikeyan, D. Kalpana and N. G. Renganathan, *Ionics*, 2009, **15**, 107-110.

32 J. B. Cheng, Y. Lu, K. W. Qiu, D. Y. Zhang, C. L. Wang, H. L. Yan, J. Y. Xu, Y. H. Zhang, X. M. Liu and Y. S. Luo, *CrystEngComm*, 2014, **16**, 9735-9742.

33 G. Q. Zhang and X. W. Lou, *Adv. Mater*., 2013, **25**, 976-979.

34 L. Yu, G. Q. Zhang, C. Z. Yuan and X. W. Lou, *Chem. Commun*., 2013, **49**, 137-139.

35 A. K. Rai, T. V. Thi, B. J. Paul and J. Kim, *Electrochim. Acta*, 2014, **146**, 577-584.

36 L. Huang, G. H. Waller, Y. Ding, D. C. Chen, D. Ding, P. X. Xi, Z. L. Wang and M. L. Liu, *Nano Energy*, 2015, **11**, 64-70.

37 W. Xiong, M. X. Liu, L. H. Gan, Y. K. Lv, Y. Li, L. Yang, Z. J. Xu, Z. X. Hao, H. L. Liu and L. W. Chen, *J. Power Sources*, 2011, **196**, 10461-10464.

38 D. Grosso, G. Illia, E. L. Crepaldi, B. Charleux and C. Sanchez, *Adv. Funct. Mater*., 2003, **13**, 37-42.

39 W. Y. Li, K. B. Xu, G. S. Song, X. Y. Zhou, R. J. Zou, J. M. Yang, Z. G. Chen and J. Q. Hu, *CrystEngComm*, 2014, **16**, 2335-2339.

40 B. A. Lu, T. Li, H. Zhao, X. Li, C. Gao, S. Zhang and E. Xie, *Nanoscale*, 2012, **4**, 2978-2982.

41 L. L. Li, S. J. Peng, Y. L. Cheah, P. F. Teh, J. Wang, G. Wee,Y. Ko, C. L. Wong and M. Srinivasan, *Chem. Eur. J*, 2013, **19**, 5892-5898.

42 Y. Yang, G. Ruan, C. Xiang, G. Wang and J. M. Tour, *J. Am. Chem. Soc*., 2014, **136**, 6187-6190.

43 S. W. Lee, J. Kim, S. Chen, P. T. Hammond and S. H. Yang, *ACS Nano*, 2010, **4**, 3889-3896.

44 B. Zhang, Y. Liu, Z. D. Huang, S. W. Oh, Y. Yu, Y. W. Mai and J. K. Kim, *J. Mater. Chem*., 2012, **22**, 12133-12140.

45 T. Yu, Y. W. Zhu, X. J. Xu, P. Chen, C. T. Lim, J. T. L. Thong and C. H. Sow, *Adv. Mater*., 2005, **17**, 1595-1599.

## Figure captions

**Fig. 1** Schematic illustrating the fabrication processes of $ZnCo_2O_4$ nanoflakes.

**Fig. 2** X-ray diffraction patterns of $ZnCo_2O_4$ and $Co_3O_4$.

**Fig. 3** (a-d) SEM images of $ZnCo_2O_4$ nanoflakes grown on a Ni foam.

**Fig. 4** (a-c) TEM images of $ZnCo_2O_4$ nanoflakes and the corresponding SAED pattern in the inset of (a); and (d) energy-dispersive X-ray spectrum of the elements Co, Zn and O.

**Fig. 5** (a) XPS spectra of $ZnCo_2O_4$ nanoflakes; and (b-d) XPS deconvoluted scans of Zn 2p, Co 2p and O 1s.

**Fig. 6** (a) CV curves for $ZnCo_2O_4$, $Co_3O_4$ and neat Ni foam electrodes, recorded at a scan of 30 mV $s^{-1}$; (b, c) CV and galvanostatic charge/discharge curves of the $ZnCo_2O_4$ electrode at different scan rates and different current densities in 2 M KOH aqueous solution, respectively; (d) specific capacitances of the $ZnCo_2O_4$ nanoflake and as-prepared $Co_3O_4$ electrodes as a function of current density.

**Fig. 7** (a) Cycling performance of the $ZnCo_2O_4$ nanoflake and as-prepared $Co_3O_4$ electrodes at a current density of 2 A $g^{-1}$; (b) rate performance of the $ZnCo_2O_4$ and $Co_3O_4$ electrodes at step-wisely increased current densities; (c) Nyquist plots of the $ZnCo_2O_4$ and $Co_3O_4$ electrodes, with the equivalent circuit in the inset; and (d) schematic representation of rechargeable supercapacitive electrode made from $ZnCo_2O_4$ nanoflakes on a Ni foam.

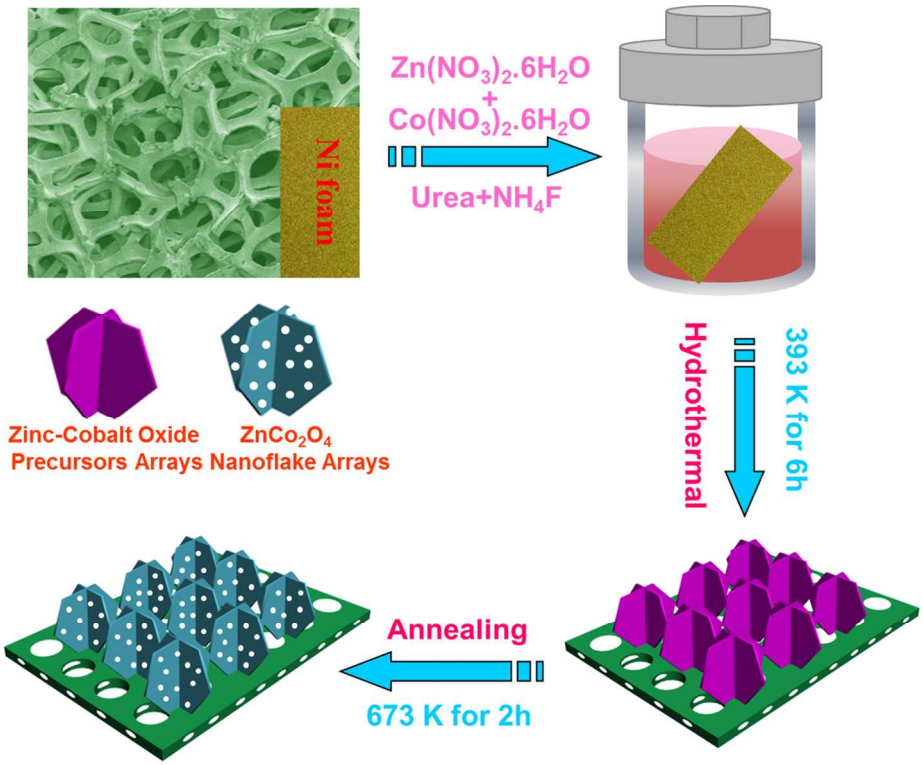


Fig 1
123x101mm (300 x 300 DPI)

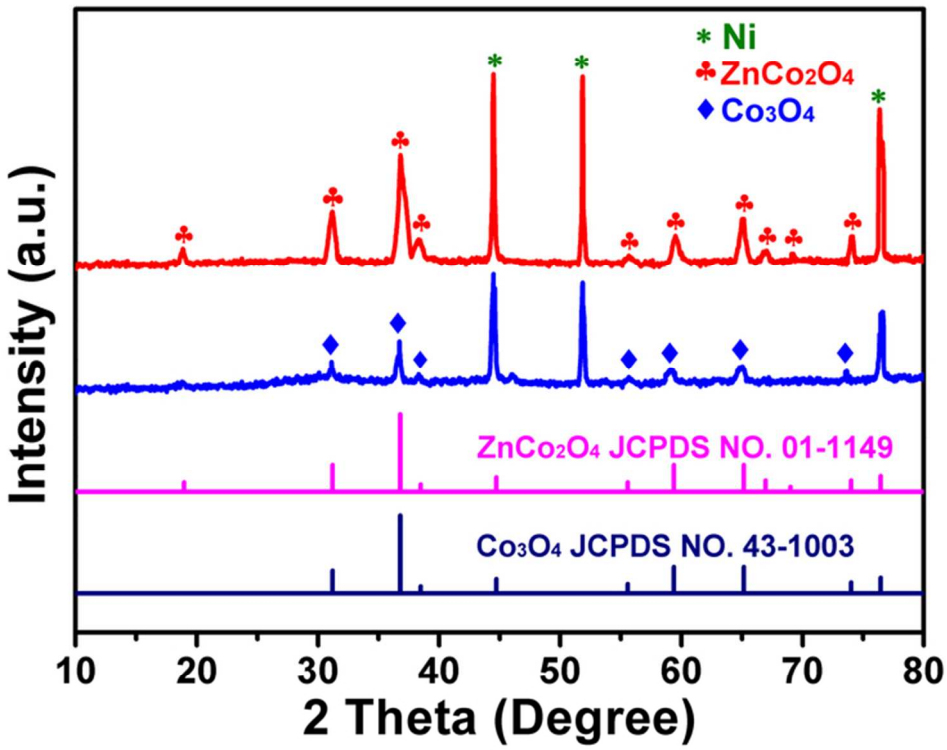


Fig 2
65x53mm (300 x 300 DPI)

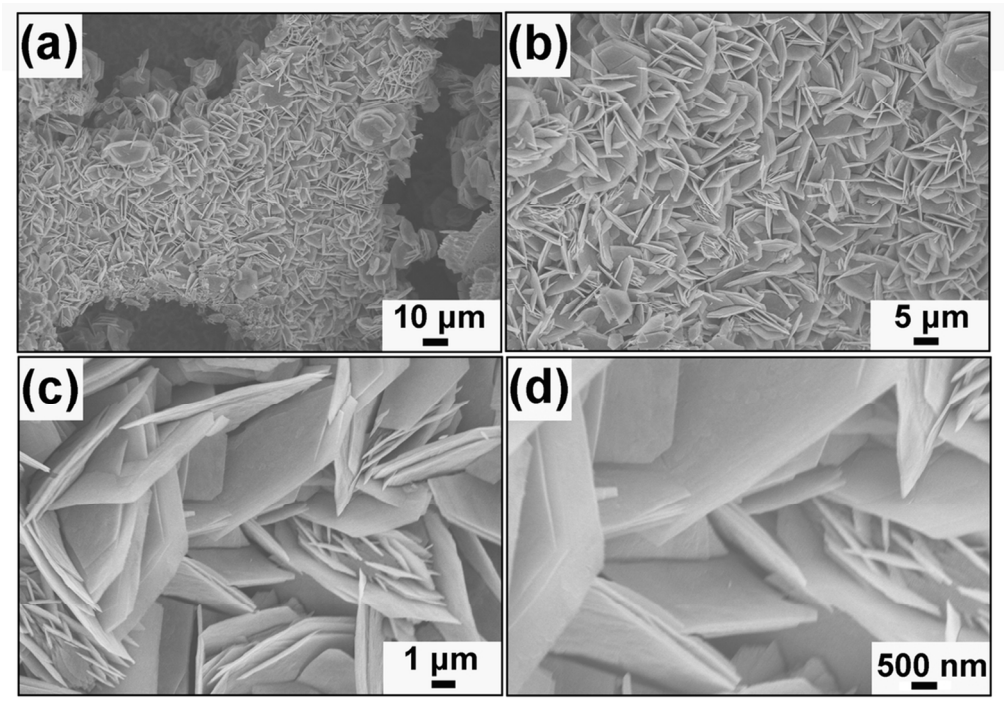


Fig 3
101x71mm (300 x 300 DPI)

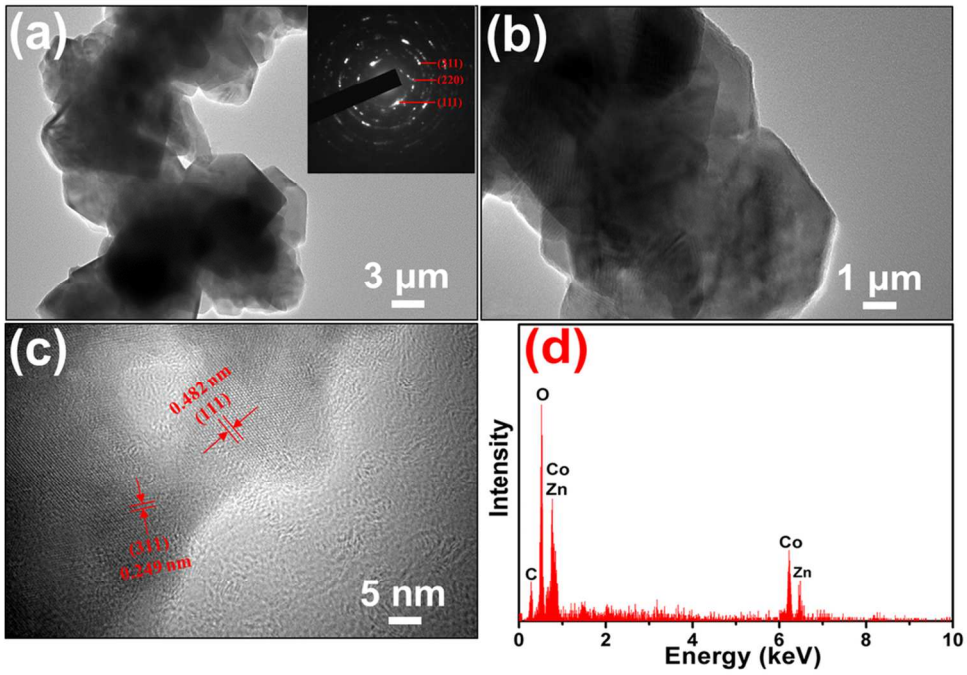


Fig 4
104x72mm (300 x 300 DPI)

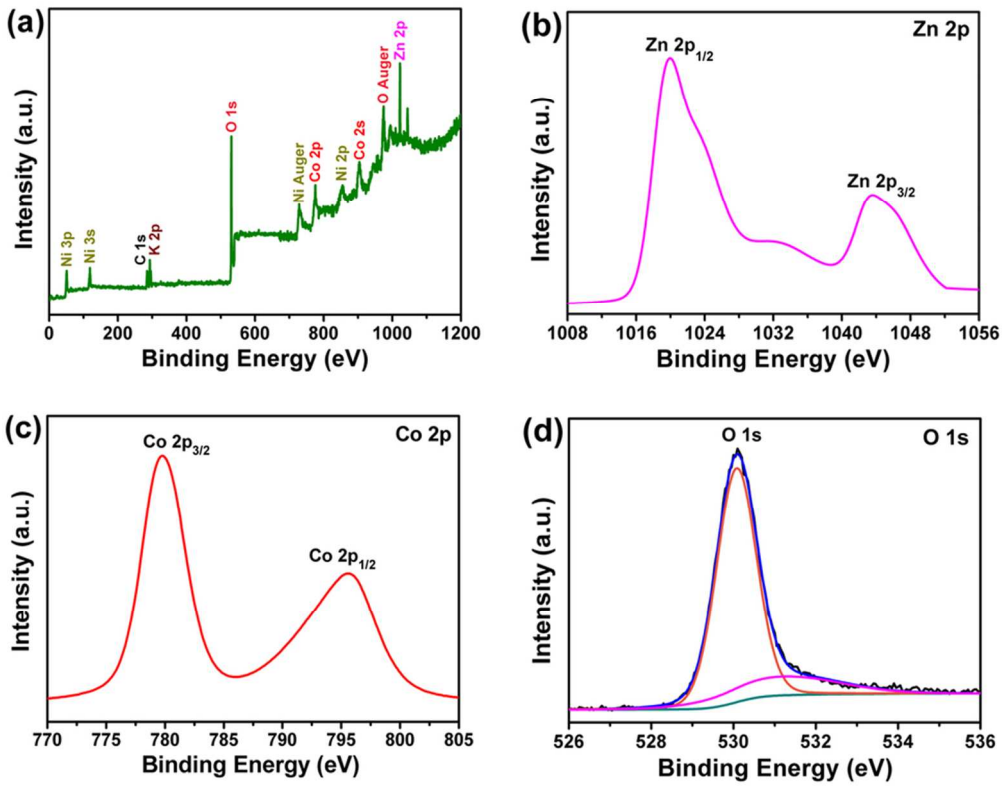


Fig 5
81x66mm (300 x 300 DPI)

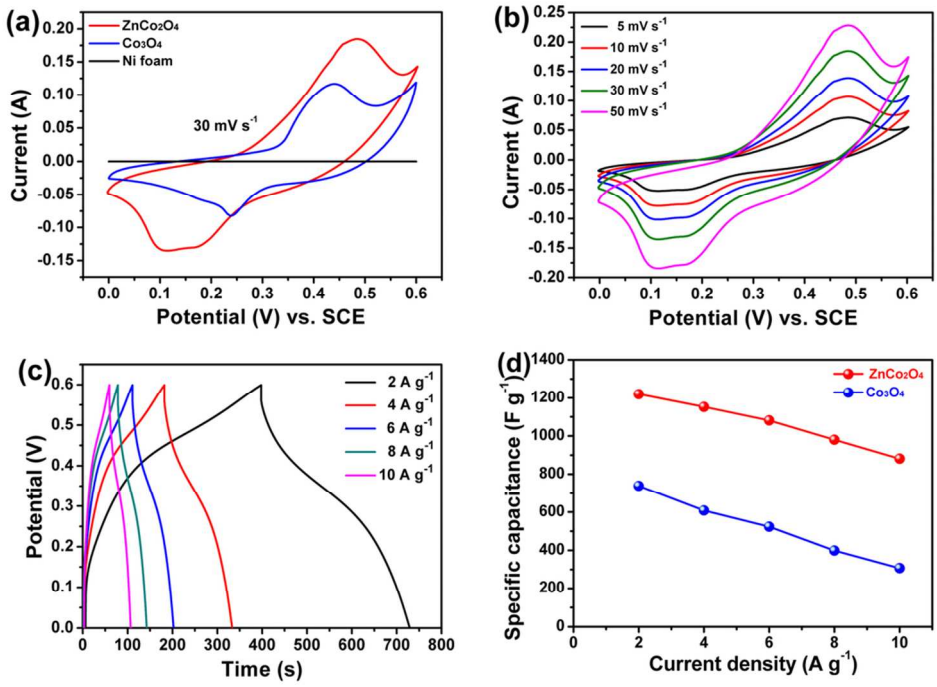


Fig 6
96x67mm (300 x 300 DPI)

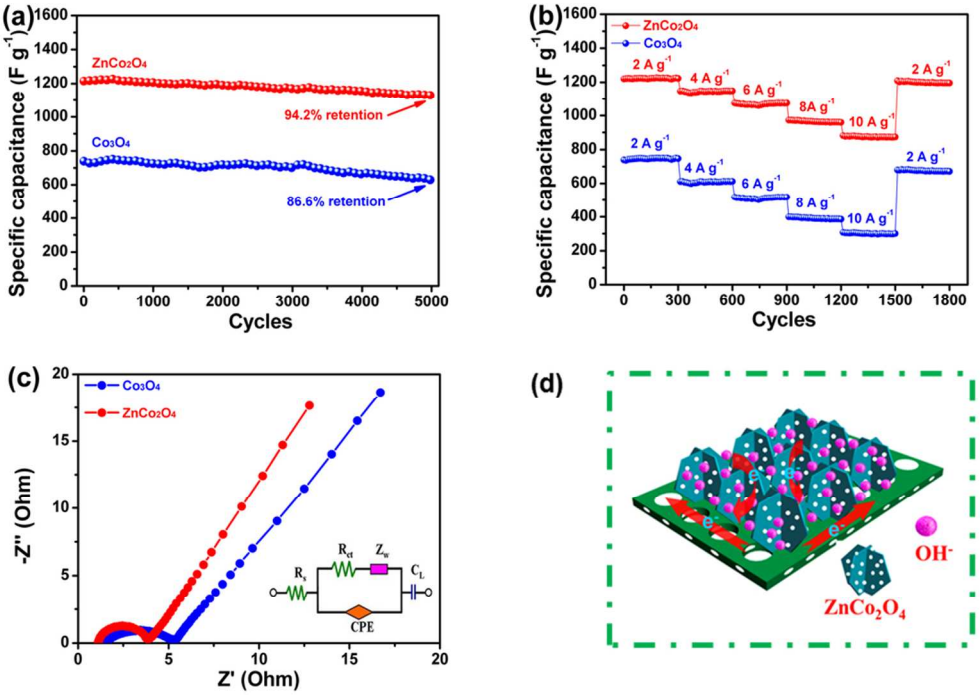


Fig 7
92x64mm (300 x 300 DPI)